Cellular and structural basis of synthesis of the unique intermediate dehydro-F_{420}-0 in mycobacteria

Rhys Grinter[1,2*], Blair Ney[1,3,4], Rajini Brammananth[1,2], Christopher K. Barlow[5,6], Paul R.F. Cordero[1,2], David L. Gillett[1,2], Thierry Izoré[5], Max J. Cryle[5], Liam K. Harold[7], Gregory M. Cook[7], George Taiaroa[8], Deborah A. Williamson[8], Andrew C. Warden[3], John G. Oakeshott[3], Matthew C. Taylor[3], Paul K. Crellin[1,2], Colin J. Jackson[4], Ralf B. Schittenhelm[5,6], Ross L. Coppel[2], Chris Greening[1,2*]

[1] School of Biological Sciences, Monash University, Clayton, VIC 3800, Australia

[2] Department of Microbiology, Monash Biomedicine Discovery Institute, Monash University, Clayton, VIC 3800, Australia

[3] CSIRO Land & Water, Canberra, ACT 2601, Australia

[4] Research School of Chemistry, Australian National University, Canberra, ACT 0200, Australia

[5] Department of Biochemistry, Monash Biomedicine Discovery Institute, Monash University, Clayton, VIC 3800, Australia

[6] Monash Proteomics & Metabolomics Facility, Monash Biomedicine Discovery Institute, Monash University, Clayton, VIC 3800, Australia

[7] Department of Microbiology and Immunology, University of Otago, Dunedin 9016, New Zealand

[8] Peter Doherty Institute for Infection and Immunity, University of Melbourne, VIC 3000, Australia

* Correspondence can be addressed to:

Associate Professor Chris Greening (chris.greening@monash.edu), School of Biological Sciences, Monash University, Clayton, VIC 3800, Australia

Doctor Rhys Grinter (rhys.grinter@monash.edu), School of Biological Sciences, Monash University, VIC 3800

Abstract

F_{420} is a low-potential redox cofactor used by diverse bacteria and archaea. In mycobacteria, this cofactor has multiple roles, including adaptation to redox stress, cell wall biosynthesis, and activation of the clinical antitubercular prodrugs pretomanid and delamanid. A recent biochemical study proposed a revised biosynthesis pathway for F_{420} in mycobacteria; it was suggested that phosphoenolpyruvate served as a metabolic precursor for this pathway, rather than 2-phospholactate as long proposed, but these findings were subsequently challenged. In this work, we combined metabolomic, genetic, and structural analyses to resolve these discrepancies and determine the basis of F_{420} biosynthesis in mycobacterial cells. We show that, in whole cells of *Mycobacterium smegmatis*, phosphoenolpyruvate rather than 2-phospholactate stimulates F_{420} biosynthesis. Analysis of F_{420} biosynthesis intermediates present in *M. smegmatis* cells harboring genetic deletions at each step of the biosynthetic pathway confirmed that phosphoenolpyruvate is then used to produce the novel precursor compound dehydro-F_{420}-0. To determine the structural basis of dehydro-F_{420}-0 production, we solved high-resolution crystal structures of the enzyme responsible (FbiA) in apo, substrate, and product bound forms. These data show the essential role of a single divalent cation in coordinating the catalytic pre-complex of this enzyme and demonstrate that dehydro-F_{420}-0 synthesis occurs through a direct substrate transfer mechanism. Together, these findings resolve the biosynthetic pathway of F_{420} in mycobacteria and have significant implications for understanding the emergence of antitubercular prodrug resistance.

Introduction

Factor 420 (F_{420}) is a deazaflavin cofactor that mediates diverse redox reactions in bacteria and archaea (1). Chemically, F_{420} consists of a redox-active deazaflavin headgroup (derived from the chromophore Fo) that is conjugated to a variable-length polyglutamate tail via a phosphoester linkage (2). While the Fo headgroup of F_{420} superficially resembles flavins (e.g. FAD, FMN), three chemical substitutions in the isoalloxazine ring give it distinct chemical properties more reminiscent of nicotinamides (e.g. NADH, NADPH) (1). These include a low standard potential (-350 mV) and obligate two-electron (hydride) transfer chemistry (3, 4). The electrochemical properties of F_{420} make it ideal to reduce a wide range of otherwise recalcitrant organic compounds (5-7). Diverse prokaryotes are known to synthesize F_{420}, but the compound is best characterised for its roles in methanogenesis in archaea, antibiotic biosynthesis in streptomycetes, and metabolic adaptation of mycobacteria (1, 8-11). In mycobacteria, F_{420} is involved in a plethora of processes: central carbon metabolism, cell wall synthesis, recovery from dormancy, resistance to oxidative stress, and inactivation of certain bactericidal agents (7, 12-14). In the human pathogen *Mycobacterium tuberculosis*, F_{420} is also critical for the reductive activation of the newly approved clinical antitubercular prodrugs pretomanid and delamanid (15-17).

Following the elucidation of the chemical structure of F_{420} in the 1970s, the F_{420} biosynthesis pathway in archaea was determined through a combination of in situ biochemistry and recombinant protein analysis (1, 2). Described briefly, the deazaflavin fluorophore Fo is synthesized through condensation of 5-amino-6-ribitylamino-2,4(1H,3H)-pyrimidinedione and L-tyrosine by the SAM-radical enzymes CofG and CofH (18). The putative enzyme CofB synthesizes 2-phospholactate (2PL), which links Fo to the glutamate tail of mature F_{420} (19). Subsequently, the nucleotide transferase CofC condenses 2PL with GTP to form the reactive intermediate L-lactyl-2-diphospho-5′-guanosine (LPPG) (20). The phosphotransferase CofD then transfers 2PL from LPPG to Fo, leading to the formation of F_{420}-0 (i.e. F_{420} with no glutamate tail) (21). Finally, the GTP-dependent glutamate ligase CofE adds a variable-length γ-linked glutamate tail to produce mature F_{420} (22, 23). With the exception of the putative lactate kinase CofB, the enzymes responsible for F_{420} biosynthesis in archaea have been identified and characterized to varying extents (1). Crystal structures have been obtained for CofC, CofD and CofE from methanogenic archaea, providing some insight into how these

87 enzymes function, but questions surrounding their catalytic mechanisms remain unresolved
88 (23-25). For example, the crystal structure of CofD from *Methanosarcina mazei* was solved in
89 the presence of Fo and GDP; however, no divalent cation(s) required for catalysis were present
90 in the structure and the ribosyl tail group of Fo, which receives the 2PL moiety from LPPG was
91 disordered, precluding an understanding of the catalytic mechanism of this step in F_{420}
92 biosynthesis (21, 25).

93 It was assumed that the biosynthesis pathway for archaeal F_{420} was generic to all F_{420} producing
94 organisms (1). However, recent studies have shown that the structure and biosynthesis of F_{420}
95 varies between producing organisms (24, 26). F_{420} produced by the proteobacterial fungal
96 symbiont *Paraburkholderia rhizoxinica* was found to incorporate 3-phospho-D-glycerate (3PG)
97 in the place of 2PL, producing a chemically distinct F_{420} (26). In parallel, analysis of purified F_{420}
98 biosynthesis enzymes from mycobacteria indicated that the central glycolytic and
99 gluconeogenic intermediate phosphoenolpyruvate (PEP), rather than 2PL, is a precursor for
100 F_{420} biosynthesis (24). In contrast to *P. rhizoxinica*, in mycobacteria, mature F_{420} is chemically
101 analogous to that produced by archaea (27). All mycobacterial species possess the four
102 enzymes required for F_{420} biosynthesis. However, as these enzymes catalyze reactions distinct
103 to their archaeal homologues, the following alternative nomenclature is applied compared to
104 the archaeal enzymes: FbiD (homologous to CofC), FbiC (a single protein with domains
105 homologous to CofG and CofH), FbiA (homologous to CofD) and FbiB (N-terminal domain
106 homologous to CofE) (8). In addition to its CofE-like domain, FbiB possesses an FMN-binding C-
107 terminal domain and biochemical evidence suggests it is responsible for the reduction of the
108 moiety derived from PEP (24, 28).

109 However, several findings have cast doubt on whether the proposed revised biosynthesis
110 pathway of F_{420} is physiologically relevant. The predicted use of PEP in F_{420} biosynthesis in
111 mycobacteria would lead to the formation of the oxidized intermediate compound dehydro-
112 F_{420}-0 (DH-F_{420}-0). The production of DH-F_{420}-0 was detected in a coupled enzyme assay
113 containing purified FbiD and FbiA with PEP supplied as the substrate but has yet to be detected
114 in mycobacterial cells (24). The study also showed that CofC from *Methanocaldococcus*
115 *jannaschii* utilized PEP rather than 2PL for F_{420} biosynthesis (24), leading the authors to
116 conclude that PEP is the general precursor for F_{420} biosynthesis in prokaryotes. However, these
117 findings contradict previous analysis of CofC activity in *M. jannaschii* cell lysates (19, 21), as

118 well as recent biochemical analysis, which shows that CofC preferentially utilizes 2PL for F_{420}
119 biosynthesis (26). In turn, these findings cast doubt on whether PEP is truly the preferred
120 substrate for mycobacterial F_{420} biosynthesis and whether DH-F_{420}-0 is the physiological
121 intermediate in this pathway.

122 In this work, we first resolved this ambiguity by analyzing the F_{420} biosynthetic pathway in *M.*
123 *smegmatis* in whole cells. We demonstrate that PEP, not 2PL, is the substrate for F_{420}
124 biosynthesis in mycobacterial cells, suggesting that divergent biosynthesis pathways are
125 utilized to generate F_{420} in different prokaryotic species. Consistent with this result, we
126 determine that DH-F_{420}-0 is the physiological intermediate for F_{420} biosynthesis in
127 mycobacteria, and is present in high quantities in cells lacking FbiB and comes bound to FbiA
128 purified from *M. smegmatis*. Furthermore, to elucidate the catalytic mechanism for the
129 formation of the novel intermediate DH-F_{420}-0, we determined the crystal structure of FbiA in
130 the presence and absence of its substrate and product compounds. These data resolve long-
131 standing questions about the catalytic mechanism of FbiA and CofD in F_{420} biosynthesis.
132 Moreover, they provide a target for therapeutic intervention through the inhibition of F_{420}
133 biosynthesis, as well as insight into potential mechanisms for the emergence of delamanid and
134 pretomanid drug resistance through mutations in FbiA.

135

136 Results

137 Phosphoenolpyruvate is the substrate for the biosynthesis of F_{420} in mycobacterial cells

138 To determine whether PEP or 2PL is the substrate for F_{420} biosynthesis in mycobacteria (Figure
139 1A), we spiked clarified cell lysates from *M. smegmatis* with GTP and either PEP or 2PL, and
140 monitored the synthesis of new F_{420} species through HPLC coupled with fluorescence detection.
141 In cell lysates spiked with PEP, a species corresponding to F_{420}-0 in the F_{420} standard was
142 present, which was absent from both the untreated and 2PL spiked lysates (Figure 1B). The
143 formation of this F_{420}-0-like species in PEP spiked lysates corresponded to a decrease in Fo
144 levels, suggesting that synthesis of DH-F_{420}-0 from PEP is occurring (Figure 1B). These data
145 strongly suggest that PEP, not 2PL, is the precursor for F_{420} biosynthesis in *M. smegmatis*.

146 While the lysate spiking experiment establishes that PEP is specifically utilised for F_{420} synthesis
147 in *M. smegmatis*, the fluorescent detection method utilised does not chemically differentiate
148 between F_{420}-0 or DH-F_{420}-0. As PEP is utilised, it would be expected that DH-F_{420}-0 is produced.
149 However, DH-F_{420}-0 may be rapidly reduced to F_{420}-0 rather than accumulating in the cell. To
150 confirm the synthesis of the DH-F_{420}-0 in *M. smegmatis*, we created isogenic deletions in the
151 four F_{420} biosynthesis genes: *fbiD*, *fbiC*, *fbiA*, and *fbiB* (Figure 2A). The genome sequences of
152 these deletion strains were determined, confirming clean deletion with no secondary
153 mutations present. We then detected the deazaflavin species present in clarified cell lysates
154 from these strains using fluorescence-coupled HPLC and LC-MS. As expected, based on the
155 proposed function of these enzymes, mature F_{420} was only detected in wild-type cell lysates
156 and possessed a polyglutamate tail length of three to eight (Figure 2B, Figure S1). Fo was
157 detected in the wildtype and all mutants with the exception of *ΔfbiC*, consistent with the
158 function of this enzyme in the synthesis of the Fo-deazaflavin moiety (Figure 2A, C, Figure S1).
159 The proposed biosynthetic intermediate DH-F_{420}-0 was detected only in cell lysates of the *ΔfbiB*
160 strain (Figure 2D, Figure S1). No F_{420}-0 was detected in wildtype or mutant strains.

161 The presence of DH-F_{420}-0 (and absence of detectable F_{420}-0) in whole cells demonstrates that
162 it is the central physiological intermediate in mycobacterial F_{420} biosynthesis. This also lends
163 support to the biochemical and cellular assays indicating that PEP, not 2PL, is the substrate for
164 this pathway in mycobacteria. Furthermore, in addition to its role as the F_{420} glutamyl-ligase,
165 structural and biochemical analysis suggests that FbiB is responsible for the reduction of DH-
166 F_{420}-0 (24, 28). The detection of DH-F_{420}-0 only in the *ΔfbiB* strain demonstrates that this
167 intermediate is rapidly turned over in the cell and supports the hypothesis that FbiB and not
168 another enzyme performs this step in mycobacterial F_{420} biosynthesis.

169

170 **FbiA co-purifies with its product dehydro-F_{420}-0**

171 In order to determine the catalytic mechanism for the synthesis of the novel intermediate DH-
172 F_{420}-0, we overexpressed and purified FbiA from *M. smegmatis*. Purified FbiA from *M.*
173 *smegmatis* possessed a light-yellow color, indicating co-purification with a product or substrate
174 molecule (Figure S2A). The nature of this substrate was investigated using fluorescence
175 spectroscopy, with purified FbiA found to have a broad absorbance peak at 400 nm and a

176 corresponding emission peak at 470 nm (Figure S2B), which is consistent with the presence of
177 a deazaflavin with a protonated 8-OH group (16). We then utilized LC/MS to identify the
178 deazaflavin species associated with FbiA and found the major species was its product DH-F_{420}-
179 0 (Figure S2C). In addition, significant quantities of mature F_{420} species were also associated
180 with FbiA, suggesting that it also binds to mature F_{420} present in the cytoplasm (Figure S2C).

181

182 **The crystal structure of FbiA reveals an active site with open and closed states**

183 In order to resolve the catalytic mechanism of DH-F_{420}-0 synthesis, purified FbiA was
184 crystallized and its structure was determined at 2.3 Å by X-ray crystallography (Table S1). FbiA
185 crystallized as a dimer mediated by the interaction of three α-helices and a β-sheet (Figure 3A).
186 This dimer is predicted to be stable by the protein-interaction prediction program PISA (29)
187 and the molecular weight of FbiA determined by SEC-MALS shows it forms a dimer in solution
188 (Table S2, Figure S2D). The structure of CofD from *M. mazei*, a homologous enzyme that
189 instead utilizes LPPG derived from 2PL as its substrate, also crystallised as a dimer with an
190 analogous interface to FbiA (25). Despite the copurification of FbiA with DH-F_{420}-0, only weak
191 electron density attributable to DH-F_{420}-0 was observed in the catalytic site of molecule B (Mol.
192 B) of the FbiA dimer (Figure S3). To obtain the product bound structure of FbiA, DH-F_{420}-0 was
193 purified from recombinant FbiA and soaked into existing crystals of FbiA. Using this procedure,
194 electron density clearly attributable to the Fo and phosphate moieties of DH-F_{420}-0 was
195 observed in Mol. B of FbiA, allowing modelling of the product bound structure (Figure S3).
196 Density for the carbonyl group of DH-F_{420}-0 was less well resolved, suggesting it exists in
197 multiple conformations in product-bound FbiA (Figure S3). Similarly, FbiA crystals were soaked
198 with Fo and GDP, individually or in combination, and structures of substrate-bound FbiA were
199 determined (Figure S3, Table S1).

200 Comparison of the Mol. A and B from the FbiA dimer reveals the active site of the enzyme in
201 distinct open and closed conformations (Figure 3). In Mol. A, the active site is locked in an open
202 state due to participation of an extended loop (amino acids 239-254) in crystal packing (Figure
203 3B). In this open state, FbiA has a lower apparent substrate affinity, with no density attributable
204 to Fo or DH-F_{420}-0 and only weak density for GDP observed in the respective co-crystal
205 structures (Figure S3). In contrast, in Mol. B the extended loop (AA 239-254) is partially

206 disordered in the non-GDP bound structures and encloses GDP in the active site in GDP-bound
207 structures (Figure 3C). In Mol. B, additional conformational changes are observed in amino
208 acids 69-102 and a subdomain composed of amino acids 145-189, creating the binding pocket
209 for the deazaflavin moiety of Fo or DH-F_{420}-0, which is not present in Mol. A (Figure 3B, C). The
210 conformational differences observed between Mol. A and Mol. B are consistent in the apo,
211 substrate and product-bound structures, demonstrating they are not substrate-induced and
212 are likely representative of conformational differences of the enzyme in solution.

213

214 **The crystal structures of FbiA in substrate- and product-bound forms provide mechanistic**
215 **insight into dehydro-F_{420}-0 synthesis**

216 The resolution of the structure of FbiA in the presence of its substrate and product compounds
217 provides key insights into the catalytic mechanism of this unique phosphotransferase. It was
218 previously established that FbiA and its archaeal homologue CofD require the presence of the
219 divalent cation Mg^{2+} for activity (21, 24). However, it remained to be resolved whether Mg^{2+} is
220 bound stably in the FbiA active site during catalysis and the mode of coordination of the ion(s).
221 In the GDP-bound structures of FbiA, a single metal ion was present in the active site of Mol. B
222 of FbiA (Figure 4A, Figure S4A, Figure S5). Interestingly, no metal ion was observed in Mol. A,
223 despite the presence of GDP, suggesting that its recruitment is conformation-dependent
224 (Figure S2). As calcium acetate is present at high concentration (0.2 M) in the crystallization
225 condition, and magnesium is absent, we modelled this ion as Ca^{2+}. While the activity of FbiA in
226 the presence of Ca^{2+} has not been tested, it has been shown to be interchangeable with Mg^{2+}
227 in some phosphotransferase and phosphohydrolase reactions (30, 31). In the GDP-only
228 structure, the Ca^{2+} ion is directly coordinated by aspartates 45 and 57, an oxygen atom of the
229 β-phosphate of GDP, two H_2O molecules, and a glycerol molecule (Figure S4B). Aspartate 57
230 exhibits bidentate coordination of the Ca^{2+} ion leading to a coordination number of seven with
231 distorted octahedral geometry.

232 In the GDP and Fo bound structure, the coordination of Ca^{2+} is analogous to the GDP-only
233 structure. However, the glycerol molecule and one of the H_2O molecules observed in the GDP
234 only structure are displaced by the ribosyl chain of Fo, resulting in a coordination number of
235 six with octahedral geometry (Figure 4B, Figure S4B). The terminal hydroxyl group of Fo is

236 significantly closer to the Ca^{2+} ion (2.6 Å) and to the β-phosphate of GDP (2.8 Å from O, and 3.0
237 Å from P) than the coordinating hydroxyl of glycerol, which is not within bonding distance of
238 GDP. These bond distances between the hydroxyl of Fo and GDP, as well as the central
239 orientation of the hydroxyl of Fo towards the β-phosphate of GDP, place it in an ideal position
240 to act as the acceptor substrate for the transfer of PEP catalysed by FbiA (Figure 4B). In the Fo
241 and DH-F_{420}-0 bound structures, no density corresponding to a Ca^{2+} ion was observed (Figure
242 4C, Figure S4C). This suggests that binding of FbiA to its catalytic metal ion is contingent on
243 complex formation with enolpyruvyl-diphospho-5′-guanosine (EPPG) (Figure 2A), which is
244 substituted for GDP in our structures due to the instability of the F_{420} pathway intermediate
245 (24). The ability of FbiA to bind Fo in the absence of GDP and Ca^{2+} suggests that substrate
246 binding to FbiA is non-sequential; however, recruitment of all three components is required
247 for catalysis to proceed.

248 Based on these structural data and previous biochemical characterization of FbiA and CofD we
249 propose a catalytic mechanism for synthesis of the DH-F_{420}-0 (Figure 4E) (21, 25). Our structural
250 data agree with previous work that suggests that CofD does not form a covalent intermediate
251 as part of the reaction mechanism (21), but rather the reaction proceeds through direct
252 nucleophilic attack of the β-phosphate of EPPG by the terminal hydroxyl of Fo. This leads to
253 the formation of a pentavalent transition state between Fo and EPPG that is stabilized by the
254 catalytic metal ion (Figure 4E). In order for the hydroxyl group of Fo to perform nucleophilic
255 attack, it needs to be activated through deprotonation. The carboxylic acid group of EPPG is a
256 likely candidate for this activation, as it is the only acidic group in close proximity to the
257 hydroxyl group of Fo when EPPG is modelled in the FbiA structure in place of GDP (Figure 4D).
258 Additionally, the activation of Fo by the carboxylic acid group of EPPG would provide FbiA with
259 substrate specificity for EPPG over GDP and GTP. Following the formation of the pentavalent
260 reaction intermediate, GMP would act as the leaving group, leading to the formation of the
261 phosphodiester bond between PEP and Fo and the formation of DH-F_{420}-0 (Figure 4E).

262

263 ## Discussion

264 Integrating these findings with other recent literature, it is now clear that the substrate for the
265 initial stage of F_{420} tail biosynthesis differs between F_{420} producing organisms (19, 24, 26). We
266 definitively show here that, in mycobacteria, PEP is the substrate for F_{420} biosynthesis,

267 resolving the ambiguity in the literature (24, 26). In contrast, in the archaeal and
268 proteobacterial species that have been analysed, 2PL and 3PG respectively are preferentially
269 utilized (19, 26). This divergent substrate utilization occurs despite the enzymes responsible
270 for this stage of synthesis (FbiD/CofC and FbiA/CofD) sharing a common evolutionary history
271 (8). This suggests that the substrate specificity of these enzymes has evolved in response to
272 selection to maintain compatibility between the substrate used for F_{420} biosynthesis and what
273 is available in the cellular metabolite pool. Both PEP and 3PG are intermediates in central
274 metabolic pathways, including glycolysis, whereas 2PL is not thought to be present in
275 significant quantities in most organisms (24, 32, 33). This makes PEP and 3PG compatible
276 substrates for F_{420} biosynthesis in *Mycobacterium* spp. and *P. rhizoxinica* respectively, with the
277 specifics of cellular metabolism of each organism likely dictating which compound was selected
278 for F_{420} biosynthesis. In contrast, in the archaeon *Methanobacterium thermoautotrophicum,*
279 2PL is present at micromolar concentrations (19). However, in archaeal species, it remains to
280 be determined how 2PL is synthesized and whether this compound plays a wider role as a
281 general metabolite beyond F_{420} biosynthesis.

282

283 Phylogenetic analysis of FbiD/CofC and FbiA/CofD suggests that these proteins were
284 horizontally transferred from bacteria and archaea (8). Based on this analysis, it is curious that
285 mycobacteria reduce DH-F_{420}-0 produced via PEP to F_{420}, rendering it chemically identical to
286 that produced with 2PL. The redox properties of the deazaflavin group of DH-F_{420} and F_{420} are
287 identical and chemically the molecules are very similar, posing the question: why is reduction
288 of DH-F_{420}-0 is required? A plausible explanation is that actinobacteria originally utilized 2PL
289 for F_{420} synthesis, with a switch to PEP occurring at a later stage in evolution. As a result, the
290 F_{420}-dependent enzymes present in mycobacteria evolved to recognize the non-planar 2PL
291 moiety of F_{420}, requiring reduction of DH-F_{420} to maintain compatibility after the substrate
292 switch. Previous structural and biochemical analysis suggests the C-terminal domain of
293 mycobacterial FbiB is responsible for the reduction of DH-F_{420}-0 (24, 28). This domain is present
294 in all mycobacterial species, but is absent from FbiB/CofE in most other F_{420} producing
295 organisms, including *M. mazei* and *P. rhizoxinica*, that produce F_{420} through pathways that do
296 not require this reductive step (8, 26). This conclusion is supported by our cellular analysis of

297 F_{420} biosynthesis in *M. smegmatis*, which shows that DH-F_{420}-0 accumulates in the *ΔfbiB* strain
298 (Figure 2A, D).

299

300 The structural analysis of FbiA that we present in this work provides unprecedented insight
301 into the catalytic mechanism for the novel phosphotransferase reaction employed at this step
302 in F_{420} biosynthesis. The crystal structure of FbiA shows that this enzyme employs a flexible
303 active site to capture Fo and EPPG, precisely positioning them for catalysis. Determination of
304 the fully resolved FbiA substrate complex, in the presence of a single catalytic metal ion,
305 provides a clear picture of the mechanism of catalysis of this enzyme. In this structure, the
306 terminal hydroxyl group of Fo is ideally positioned for nucleophilic attack of the β-phosphate
307 of EPPG, strongly suggesting that DH-F_{420}-0 biosynthesis occurs through direct transfer of PEP
308 to Fo, via a pentavalent phosphate intermediate that is stabilized by the catalytic metal ion.
309 The positioning of the Fo terminal hydroxyl group in our structure in relation to EPPG is
310 strikingly similar to that of the attacking ribose in the final step in DNA ligation by T4 ligase,
311 recently resolved by X-ray crystallography (34). This is consistent with both reactions resulting
312 in the formation of a phosphodiester bond through direct nucleophilic attack of a
313 diphosphonucleoside intermediate. As no acidic side chains are present in proximity the
314 terminal hydroxyl of Fo in our structure of FbiA, it is likely that deprotonation of this group for
315 nucleophilic attack is EPPG induced, possibly by the PEP carboxyl moiety. These data are also
316 consistent with biochemical analysis of CofD from *M. mazei*, which did not detect the
317 formation of a catalytic reaction intermediate during the synthesis of F_{420}-0 (21).

318

319 The resolution of the F_{420} biosynthesis pathway also has implications for tuberculosis
320 treatment. It has been proposed that F_{420} biosynthesis represents a promising target for the
321 development of drugs for the treatment of *M. tuberculosis* given the pleiotropic role of this
322 cofactor and its absence from human cells. Given FbiA mediates the key step in F_{420}
323 biosynthesis, the structural insights into FbiA catalysis provide a basis for the development of
324 inhibitory compounds targeting F_{420} biosynthesis. In addition, loss-of-function of FbiA causes
325 resistance to the clinical nitroimidazole prodrugs delamanid and pretomanid, both of which
326 are activated by the $F_{420}H_2$-dependent reductase Ddn (15, 17, 35). Hence, the structural and

327 mechanistic insights provided here will enable prediction of which substitutions are likely to
328 impair or inactivate FbiA, thus conferring resistance to these compounds.

329

330 ## Methods

331 ### Creation of *M. smegmatis* F_{420} biosynthesis mutant strains

332 *M. smegmatis* MSMEG_5126 was deleted in wild-type *M. smegmatis* mc^2 155 using a two-step
333 allelic replacement strategy. Two 0.8 kb fragments containing sequences from the left and right
334 flanking regions of the MSMEG_5126 (*fbiC*) gene were cloned as separate constructs and later
335 combined to make the deletion construct. The left flanking fragments were amplified using
336 ProofStart DNA polymerase (Qiagen) with primers MSMEG_5126left and MSMEG_5126leftrev,
337 and the PCR product was subsequently cloned into the SacI/BamHI sites of pUC18, creating
338 plasmid pUC-MSMEG_5126left (primers described in Table S3). A 0.8 kb fragment containing
339 sequence from the right side of MSMEG_5126 was amplified using primers MSMEG_5126right
340 and MSMEG_5126rightrev and cloned into the XbaI/BamHI sites of pUC18, creating plasmid
341 pUC-MSMEG_5126right. The right flanking sequence was then excised from pUC-
342 MSMEG_5126right using XbaI/SacI and subcloned into Xba/SacI-digested pUC-
343 MSMEG_5126left, fusing the left and right flanking sequences to create plasmid pUC-
344 ΔMSMEG_5126.

345 The 1.6 kb fused insert was then liberated using Xba/SacI and subcloned into Xba/SacI-digested
346 pMSS vector (36), a suicide plasmid for *M. smegmatis* that contains streptomycin selection and
347 sucrose contra-selection markers. The resultant plasmid, pMSS:ΔMSMEG_5126, was
348 sequenced then electroporated into electrocompetent *M. smegmatis* $mc^2$155 cells, using an
349 ECM 630 electroporator (BTX), selecting for streptomycin-resistant colonies (30 µg/ml), which
350 were then screened for sensitivity to 10% (w/v) sucrose. DNA from confirmed streptomycin-
351 resistant, sucrose-sensitive colonies was PCR amplified using primer pair MSMEG_5126screen-
352 F and MSMEG_5126KOright-R. The resultant PCR product was confirmed by DNA sequencing.

353 A confirmed single crossover (SCO) strain was grown for three days in the absence of antibiotic
354 selection, serially diluted and plated on LB plates containing 10% (w/v) sucrose to select for
355 potential double crossover (DCO) strains (*ie*. MSMEG_5126 deletion mutants). Genomic DNA
356 was extracted from sucrose-resistant, streptomycin-sensitive clones, digested using ClaI/NcoI

357 and subjected to Southern blot analysis using an MSMEG_5126 specific probe to confirm
358 deletion of the MSMEG_5126 gene. For Southern blotting analysis 2 µg of gDNA was digested
359 with appropriate restriction enzymes (NEB) at 37 °C for 16 hours. Purified samples and
360 digoxygenin (DIG)-labeled, HindIII-digested λ DNA markers were separated on a 1% agarose gel
361 followed by depurination, denaturation, neutralization, and capillary transfer onto a nylon
362 membrane (Thermo Fisher). The membrane was then hybridized at 67 °C with a gene-specific
363 probe prepared by DIG labelling a 3.0-kb PCR product obtained using primers
364 MSMEG_5126screen-R and MSMEG_5126screen-F. Once confirmed by Southern blotting, the
365 genome of a mutant was sequenced at The Peter Doherty Institute for Infection and Immunity
366 at the University of Melbourne.

367 MSMEG_1829 (*fbiB*), MSMEG_2392 (*fbiD*) and MSMEG_1830 (*fbiA*) deletion mutants were
368 generated following the same methods as MSMEG_5126, using gene-specific primer
369 combinations (Table S3). Individual deletion mutants of *fbiA*, *fbiB* and *fbiD* were confirmed by
370 Southern blot following digestion with PvuII and then genome sequencing.

371

372 **Purification of Fo, DH-F_{420}-0 and F_{420}**

373 Fo was purified from culture supernatants of *M. smegmatis* mc^2155 overexpressing FbiC from
374 *M. tuberculosis* cloned into the acetamide inducible vector pMyNT. Cells were grown at 37 °C
375 in 7H9 media to an OD_{600} ~3.0 before FbiC expression was induced by the addition of 0.2 %
376 acetamide. Cells were grown for an additional 72 hours at 37 °C with shaking and supernatant
377 was clarified by centrifugation at 10,000 x g for 20 minutes. The clarified supernatant was
378 filtered (0.45 µM) and applied to a C18-silica column equilibrated in dH_2O. Bound Fo was eluted
379 with 20 % methanol in dH_2O and the solvent was removed by vacuum evaporation. Fo was
380 resuspended in dH_2O and centrifuged (20,000 g for 20 minutes) to remove insoluble
381 contaminants, before reapplication to a C18-silica column equilibrated in dH_2O. Fo was again
382 eluted with 20 % methanol in dH_2O, vacuum evaporated and stored at -20 °C for further
383 analysis.

384 F_{420} was expressed and purified as previously described in *M. smegmatis* mc^24517
385 overexpressing FbiA, FbiB, and FbiC in the expression vector pYUBDuet-FbiABC (37). Cells were
386 grown in LB broth + 0.05% Tween 80 at 37 °C with shaking to an OD_{600} of ~2.0 before the

387 expression of the *fbi* genes was induced with 0.2 % acetamide. Cells were grown for an
388 additional 72 hours before harvesting by centrifugation at 10,000 × *g* for 20 minutes. Cells were
389 resuspended in 50 mM Tris (pH 7.5) at a ratio of 10 ml of buffer per 1 gram of wet cells and
390 lysed by autoclaving. The autoclaved cell suspension was clarified by centrifugation at 20,000
391 × *g* for 20 minutes. The clarified supernatant was applied to a High Q Anion Exchange Column
392 (Biorad) equilibrated in 50 mM Tris (pH 7.5). Bound species were eluted with a gradient of 0-
393 100 % of 50 mM Tris, 1 M NaCl (pH 7.5). Fractions containing F_{420} were identified via visible
394 spectroscopy based on their distinctive absorbance peak at 420 nm. Fractions containing F_{420}
395 were pooled and applied to a C18-silica column equilibrated in dH_2O. F_{420} was eluted with 20 %
396 methanol in H_2O, vacuum evaporated and stored at -20 °C for further analysis.

397 DH-F_{420}-0 was extracted from purified FbiA expressed in *M. smegmatis* as described below.
398 Purified concentrated FbiA (~20 mg ml^{-1}; prior to cleavage of the poly-histidine tag) was
399 denatured in a buffer containing 50 mM Tris and 8 M Urea (pH 7.0). This solution containing
400 denatured FbiA and free DH-F_{420}-0 was applied to a nickel-agarose column, with denatured
401 FbiA binding to the column due to its hexahis-tag and DH-F_{420}-0 eluting in the flowthrough. The
402 flowthrough containing DH-F_{420}-0 was applied to a Superdex 30 10/300 column equilibrated in
403 dH_2O and eluted fractions containing DH-F_{420}-0 were identified based on their absorbance at
404 420 nM. DH-F_{420}-0 containing fractions were pooled, vacuum evaporated, resuspended in 500
405 µl of dH_2O and reapplied to the Superdex 30 10/300 column equilibrated in 20 % acetonitrile
406 in dH_2O. DH-F_{420}-0 containing fractions were then pooled, vacuum evaporated and stored at -
407 20 °C for further analysis.

408

409 **FbiA expression and purification**

410 The DNA coding sequence corresponding to FbiA from *M. smegmatis* was amplified by PCR
411 using primers outlined in Table S3, resulting in a DNA fragment with 5' NcoI and 3' HindIII sites
412 respectively. This fragment was cloned into pMyNT by restriction enzyme cloning using the
413 aforementioned sites, yielding pMyNTFbiAMS, which expresses FbiA with a TEV cleavable N-
414 terminal hexahistidine tag. This vector was cloned and propagated in *E. coli* DH5α in LB
415 media/agar with the addition of 200 µg ml^{-1} hygromycin B. Sequence confirmed pMyNTFbiAMS
416 was transformed into *M. smegmatis* mc^2155 via electroporation, with successful transformants

417 selected for in LB + 0.05 % Tween 80 (LBT) agar in the presence of 50 µg ml^{-1} hygromycin B.
418 Colonies from this transformation were used to inoculate 50 ml of LBT media +50 µg ml^{-1}
419 hygromycin B, which was grown with shaking at 37 °C until stationary phase (2-3 days). This
420 starter culture was used to inoculate 5 liters of Terrific Broth + 0.05 % Tween 80 (TBT) giving a
421 1:100 dilution of the starter culture. Cells were grown with shaking at 37 °C for 24 hours until
422 approximately mid-log phase and protein production was induced through the addition of 0.2%
423 acetamide. Cells were grown with shaking at 37 °C for an additional 72 hours before they were
424 harvested via centrifugation at 5,000 × *g* for 20 minutes. Harvested cells were either lysed
425 immediately or stored frozen at -20 °C.

426 Cells were resuspended in Ni binding buffer (20 mM HEPES, 300 mM NaCl, 20 mM imidazole;
427 pH 7.5) at a ratio of approximately 5 ml of buffer per 1 g of wet cell mass. Lysozyme (1 mg ml^{-}
428 ^{1}), DNAse (0.5 mg ml^{-1}) and complete protease inhibitor tablets (Roche) were added and cells
429 were lysed with a cell disruptor (Constant Systems). The cell lysate was stored on ice and
430 clarified by centrifugation at 4 °C at 30,000 × *g*. Clarified lysate was passed through a column
431 containing Ni^{2+} agarose resin equilibrated in Ni binding buffer. The column was washed with Ni
432 binding buffer and protein was eluted with a gradient of Ni Gradient Buffer (20 mM HEPES,
433 300 mM NaCl, 500 mM imidazole; pH 7.5). Fractions containing FbiA were identified based on
434 absorbance at 280 nm and their yellow color due to F_{420} precursor co-purification and pooled.
435 Pooled fractions were applied a Superedex S200 26/600 size exclusion chromatography (SEC)
436 column, equilibrated with SEC buffer (20 mM HEPES, 150 mM NaCl; pH 7.5), and fractions
437 containing FbiA were identified as above and pooled. The hexahis-tag was cleaved from
438 purified FbiA through the addition of 0.5 mg of hexahistidine-tagged TEV protease (expressed
439 and purified as described in reference (38)) per mg of FbiA, plus 1 mM DTT. Digestion was
440 performed at room temperature for ~6 hours before the sample was passed through a Ni^{2+}
441 agarose column to remove TEV and the cleaved hexahis tag. The resulting flowthrough from
442 this column was collected, concentrated to ~15 mg ml^{-1} and snap frozen at -80 °C. Purified FbiA
443 was lightly yellow in color due to co-purification with F_{420} precursors, with a yield of 5-10 mg
444 per litre of culture. The molecular weight of purified FbiA was determined by size exclusion
445 coupled multiangle laser light scattering (SEC-MALS), using a Superdex S200 Increase 10/300
446 column equilibrated in 200 mM NaCl, 50 mM Tris [pH 7.9], coupled to FPLC (Shimadzu) with
447 MALS detection (Wyatt Technology).

448

449 FbiA crystallisation, ligand soaking and structure solution

450 Purified FbiA was screened for crystallisation conditions using a sparse matrix approach, with
451 approximately 600 individual conditions screened. Thin inter-grown plate crystals of FbiA
452 formed in a number of conditions, with a condition containing 0.1 M Tris (pH 8.0), 0.2 M Ca
453 Acetate and 20 % PEG 3350 chosen for optimization. Diffraction quality crystals were obtained
454 by microseeding into 0.1 M Tris (pH 8.5), 0.2 M Ca Acetate and 16 % PEG 3350 +/- 20 % glycerol.
455 Crystals grew as bunches of very thin plates and were slightly yellow in color. Crystals from
456 conditions containing glycerol were looped and directly flash cooled to 100 K in liquid N_2,
457 providing 'apo' crystals for data collection. Crystals from non-glycerol containing wells were
458 transferred into well solution with 20 % glycerol and either Fo, GDP, Fo and GDP or DH-F_{420}-0.
459 Crystals were incubated in this solution for 1-5 minutes before they were looped and flash
460 cooled to 100 K in liquid N_2.

461 Data were collected at the Australian Synchrotron, with crystals diffracting anisotropically to
462 ~2.2 to 3.0 Å, and processed using XDS and merged using Aimless from the CCP4 package (39,
463 40). The structure of FbiA was solved by molecular replacement using Phaser (41), with a
464 search model derived from the structure of CofD from *M. mazei* (PDB ID: 3C3D) prepared based
465 on the amino acid sequence for FbiA from *M. smegmatis* using sculptor from the Phenix
466 package (41). Native and ligand soaked structures of FbiA were built and refined using Coot
467 and phenix.refine from the Phenix package (41, 42). Structural coordinates for Fo, DH-F_{420}-0
468 and F_{420} were generated using the AceDrg program within the CCP4 suite (40, 43).

469

470 LC-MS detection of F_{420} and precursors

471 Wild-type and Fbi mutant *M. smegmatis* mc^2155 strains were grown in 20 ml of LBT media
472 until stationary phase (2-3 days) and harvested by centrifugation at 5,000 × *g* for 20 minutes.
473 Cells were resuspended in 2 ml of dH_2O and lysed by boiling for 5 minutes before clarification
474 by centrifugation at 25,000 × *g* for 10 minutes. The soluble fraction was then decanted for
475 mass spectrometry analysis. Samples were analyzed by hydrophilic interaction liquid
476 chromatography (HILIC) coupled to high-resolution mass spectrometry (LC−MS) according to a

477 previously published method (44). In brief, the chromatography utilized a 20 × 2.1 mm guard
478 in series with a 150 × 4.6 mm analytical column (both ZIC-pHILIC, Merck). Column temperature
479 was maintained at 25 °C with a gradient elution of 20 mM ammonium carbonate (A) and
480 acetonitrile (B) (linear gradient time-%B as follows: 0 min-80%, 15 min-50%, 18 min-5%, 21
481 min-5%, 24 min-80%, 32 min-80%) on a Dionex RSLC3000 UHPLC (Thermo). The flow rate was
482 maintained at 300 µl min^{-1}. Samples were kept at 4 °C in the autosampler and 10 µl was injected
483 for analysis. The mass spectrometric acquisition was performed at 35,000 resolution on a Q-
484 Exactive Orbitrap MS (Thermo) operating in rapid switching positive (4 kV) and negative (−3.5
485 kV) mode electrospray ionization (capillary temperature 300 °C; sheath gas 50; Aux gas 20;
486 sweep gas 2; probe temp 120 °C). The resulting LC-MS data were processed by integrating the
487 area below the extracted ion chromatographic peaks using TraceFinder 4.1 (Thermo Scientific).
488 All species were detected in negative mode as the singly deprotonated anion (Fo and DH-F_{420}-
489 0) or in the case of the F_{420}-n species the double deprotonated dianion.

490

491 2PL synthesis

492 2PL was chemically synthesized using the following protocol: Benzyl lactate was condensed
493 with chlorodiphenyl phosphate in pyridine, with cooling, to give benzyldiphenylphosphoryl
494 lactate. Hydrogenolysis of this material in 70% aqueous tetrahydrofuran over 10% Palladium
495 on carbon (Pd-C) gave phospholactic acid as a colorless, viscous oil, which was characterized
496 by proton, carbon and phosphorus NMR spectroscopy, and by mass spectrometry. ^{1}H NMR
497 (DMSO-d6) δ 11.68 (br, 3H), 4.53 (m, 1H), 1.36 (d, J=6.8 Hz, 3H). ^{13}C NMR (DMSO-d6) δ 172.50
498 (d, JP-C=0.05 Hz), 69.56 (d, JP-C=0.04 Hz), 19.27 (d, JP-C=0.04 Hz). ^{31}P NMR (DMSO-d6) δ -1.64.
499 APCI-MS found: [M+H]+=171.1, [M-H]-=169.1.

500

501 Stimulation of DH-F_{420}-0 production in spiked *M. smegmatis* cell lysates and detection of F_{420}
502 species by HPLC

503 To detect F_{420} synthesis in spiked *M. smegmatis* lysates, 500 ml cultures were grown in LBT for
504 3 days at 37 °C with shaking. Cells were harvested by centrifugation at 8,000 × *g* for 20 min,
505 4 °C. The pellet was resuspended in 50 ml lysis buffer (50 mM MOPS, 1 mM

506 phenylmethylsulfonyl fluoride (PMSF), 1 mM DTT, 5 mM $MgCl^2$, 2.5 $mg.ml^{-1}$ lysozyme, 2.5 mg
507 Deoxyribonuclease I). An M-110P Microfluidizer (Fluigent) pressure-lysis maintained at 4 °C
508 was used to lyse the cells. The lysate was centrifuged at 10,000 × *g* at 4 °C for 20 min. 1 ml
509 aliquots of lysate were spiked with either 1 mM phosphate buffer (pH 7.0) plus GTP and 2PL,
510 or GTP and PEP. These spiked samples, along with a 'no spike' control, were incubated at 4
511 hours at 37 °C. To terminate the reaction, the aliquots were heated at 95 °C for 20 min, then
512 centrifuged at 16,000 × *g* for 10 min. The supernatants were filtered through a 0.22 µm PVDF
513 filter and moved to analytical vials.

514 F_{420} biosynthetic intermediates present in the filtered *M. smegmatis* cell lysates were analysed
515 by separation and detection using an Agilent 1200 series HPLC system equipped with a
516 fluorescence detector and a Poroshell 120 EC-C18 2.1 x 50 mm 2.7 µm column. The system
517 was run at a flow rate of 0.3 ml min^{-1} and the samples were excited at 420 nm and emission
518 was detected at 480 nm. A gradient of two buffers were used: Buffer A, containing 20 mM
519 ammonium phosphate, 10 mM tetrabutylammonium phosphate, pH 7.0. Buffer B, 100%
520 acetonitrile. A gradient was run from 25% to 40% buffer B as follows: 0-1 min 25%, 1-10 min
521 25%-35%, 10-13 min 35%, 13-16 min 35-40%, 16-19 min 40%-25%.

522

Acknowledgements

This research was undertaken in part using the MX2 beamline at the Australian Synchrotron, part of ANSTO, and made use of the Australian Cancer Research Foundation (ACRF) detector. We would like to thank the Monash Crystallisation Facility for their assistance with sample characterization, crystallographic screening, and optimization. pMyNT was a gift from Dr. Katherine Beckham, Dr. Annabel Parret, and Prof. Matthias Wilmanns at EMBL Hamburg. This work was supported by an ARC DECRA Fellowship (DE170100310; awarded to C.G.), an NHMRC EL2 Fellowship (APP1178715; awarded to C.G.), an NHMRC New Investigator Grant (APP5191146; awarded to C.G.), an NHMRC grant (APP1139832; awarded to C.J.J., C.G., and G.M.C.), a Monash University Science-Medicine Seed Grant (awarded to C.G. and M.J.C.), and Monash University Doctoral Scholarships (awarded to P.R.F.C. and D.G), an ARC Discovery Grant (DP180102463; awarded to R.L.C.) We would like to thank Dr. Ghader Bashiri for helpful discussions, Dr. Matthew Belousoff for his assistance in the development of F_{420} derivative purification protocols, and Mr. Phillip Holt in the School of Chemistry, Monash University for his assistance with Fluorescence HPLC analysis.

Author contributions

C.G. and R.G. conceived and supervised the study. Different authors contributed to cellular spiking assays (B.N., C.G., C.J.J., A.W., M.C.T.), knockout construction (C.G., R.B., R.L.C., P.K.C., G.M.C., J.G.O., M.C.T., L.K.H., G.T., D.A.W.), LC-MS analysis (C.K.B., R.G., R.S., C.G.), protein purification (R.G., C.G., B.N., P.R.F.C., C.J.J.), and crystallographic analysis (R.G., P.R.F.C., D.L.G., C.G., T.I., M.J.C.). R.G. and C.G. analysed data and wrote the paper with input from all authors.

Competing financial interests

The authors declare no competing financial interests.

References

1. Greening C*, et al.* (2016) Physiology, biochemistry, and applications of F420-and Fo-dependent redox reactions. *Microbiol. Mol. Biol. Rev.* 80(2):451-493.
2. Eirich LD, Vogels GD, & Wolfe RS (1978) Proposed structure for coenzyme F420 from *Methanobacterium*. *Biochemistry* 17(22):4583-4593.
3. Jacobson F & Walsh C (1984) Properties of 7, 8-didemethyl-8-hydroxy-5-deazaflavins relevant to redox coenzyme function in methanogen metabolism. *Biochemistry* 23(5):979-988.
4. Edmondson DE, Barman B, & Tollin G (1972) Importance of the N-5 position in flavine coenzymes. Properties of free and protein-bound 5-deaza analogs. *Biochemistry* 11(7):1133-1138.
5. Taylor MC*, et al.* (2010) Identification and characterization of two families of F420H2-dependent reductases from Mycobacteria that catalyse aflatoxin degradation. *Mol. Microbiol.* 78(3):561-575.
6. Li W, Khullar A, Chou S, Sacramo A, & Gerratana B (2009) Biosynthesis of sibiromycin, a potent antitumor antibiotic. *Appl. Environ. Microbiol.* 75(9):2869-2878.
7. Greening C*, et al.* (2017) Mycobacterial $F_{420}H_2$-dependent reductases promiscuously reduce diverse compounds through a common mechanism. *Frontiers in microbiology* 8:1000.
8. Ney B*, et al.* (2017) The methanogenic redox cofactor F 420 is widely synthesized by aerobic soil bacteria. *The ISME journal* 11(1):125.
9. Rinke C*, et al.* (2013) Insights into the phylogeny and coding potential of microbial dark matter. *Nature* 499(7459):431.
10. Wu D*, et al.* (2009) A phylogeny-driven genomic encyclopaedia of Bacteria and Archaea. *Nature* 462(7276):1056.
11. Spang A*, et al.* (2012) The genome of the ammonia-oxidizing Candidatus *Nitrososphaera gargensis*: insights into metabolic versatility and environmental adaptations. *Environmental microbiology* 14(12):3122-3145.
12. Gurumurthy M*, et al.* (2013) A novel F420-dependent anti-oxidant mechanism protects *M ycobacterium tuberculosis* against oxidative stress and bactericidal agents. *Mol. Microbiol.* 87(4):744-755.
13. Jirapanjawat T*, et al.* (2016) The redox cofactor F420 protects mycobacteria from diverse antimicrobial compounds and mediates a reductive detoxification system. *Appl. Environ. Microbiol.* 82(23):6810-6818.
14. Purwantini E & Mukhopadhyay B (2013) Rv0132c of *Mycobacterium tuberculosis* encodes a coenzyme F420-dependent hydroxymycolic acid dehydrogenase. *PloS one* 8(12):e81985.
15. Cellitti SE*, et al.* (2012) Structure of Ddn, the deazaflavin-dependent nitroreductase from *Mycobacterium tuberculosis* involved in bioreductive activation of PA-824. *Structure* 20(1):101-112.
16. Mohamed A*, et al.* (2016) Protonation state of F420H2 in the prodrug-activating deazaflavin dependent nitroreductase (Ddn) from *Mycobacterium tuberculosis*. *Mol. Biosyst.* 12(4):1110.
17. Lee BM*, et al.* (2019) The evolution of nitroimidazole antibiotic resistance in Mycobacterium tuberculosis. *bioRxiv*:631127.
18. Graham DE, Xu H, & White RH (2003) Identification of the 7, 8-didemethyl-8-hydroxy-5-deazariboflavin synthase required for coenzyme F 420 biosynthesis. *Arch. Microbiol.* 180(6):455-464.
19. Graupner M & White RH (2001) Biosynthesis of the phosphodiester bond in coenzyme F420 in the methanoarchaea. *Biochemistry* 40(36):10859-10872.
20. Grochowski LL, Xu H, & White RH (2008) Identification and characterization of the 2-phospho-L-lactate guanylyltransferase involved in coenzyme F420 biosynthesis. *Biochemistry* 47(9):3033-3037.

600 21. Graupner M, Xu H, & White RH (2002) Characterization of the 2-phospho-L-lactate
601 transferase enzyme involved in coenzyme F420 biosynthesis in *Methanococcus jannaschii*.
602 *Biochemistry* 41(11):3754-3761.
603 22. Li H, Graupner M, Xu H, & White RH (2003) CofE catalyzes the addition of two glutamates to
604 F420-0 in F420 coenzyme biosynthesis in *Methanococcus jannaschii*. *Biochemistry*
605 42(32):9771-9778.
606 23. Nocek B*, et al.* (2007) Structure of an amide bond forming F420: γγ-glutamyl ligase from
607 Archaeoglobus fulgidus-a member of a new family of non-ribosomal peptide synthases. *J.*
608 *Mol. Biol.* 372(2):456-469.
609 24. Bashiri G*, et al.* (2019) A revised biosynthetic pathway for the cofactor F 420 in prokaryotes.
610 *Nat. Commun.* 10(1):1558.
611 25. Forouhar F*, et al.* (2008) Molecular insights into the biosynthesis of the F420 coenzyme. *J.*
612 *Biol. Chem.* 283(17):11832-11840.
613 26. Braga D*, et al.* (2019) Metabolic Pathway Rerouting in *Paraburkholderia rhizoxinica* Evolved
614 Long-Overlooked Derivatives of Coenzyme F420. *ACS Chem. Biol.*
615 27. Bair TB, Isabelle DW, & Daniels L (2001) Structures of coenzyme F_{420} in *Mycobacterium*
616 species. *Arch. Microbiol.* 176(1-2):37-43.
617 28. Bashiri G*, et al.* (2016) Elongation of the poly-γ-glutamate tail of F420 requires both domains
618 of the F420: γ-glutamyl ligase (FbiB) of *Mycobacterium tuberculosis*. *J. Biol. Chem.*
619 291(13):6882-6894.
620 29. Krissinel E & Henrick K (2007) Inference of macromolecular assemblies from crystalline state.
621 *Journal of molecular biology* 372(3):774-797.
622 30. Grinter R, Roszak AW, Cogdell RJ, Milner JJ, & Walker D (2012) The crystal structure of the
623 lipid II-degrading bacteriocin syringacin M suggests unexpected evolutionary relationships
624 between colicin M-like bacteriocins. *Journal of Biological Chemistry* 287(46):38876-38888.
625 31. Knape MJ*, et al.* (2015) Divalent metal ions Mg^{2+} and Ca^{2+} have distinct effects on protein
626 kinase A activity and regulation. *ACS chemical biology* 10(10):2303-2315.
627 32. Braga D*, et al.* (2019) Metabolic pathway rerouting in *Paraburkholderia rhizoxinica* evolved
628 long-overlooked derivatives of coenzyme F420. *bioRxiv*:670455.
629 33. Fothergill-Gilmore LA & Michels PA (1993) Evolution of glycolysis. *Progress in biophysics and*
630 *molecular biology* 59(2):105-235.
631 34. Shi K*, et al.* (2018) T4 DNA ligase structure reveals a prototypical ATP-dependent ligase with
632 a unique mode of sliding clamp interaction. *Nucleic acids research* 46(19):10474-10488.
633 35. Haver HL*, et al.* (2015) Mutations in genes for the F420 biosynthetic pathway and a
634 nitroreductase enzyme are the primary resistance determinants in spontaneous in vitro-
635 selected PA-824-resistant mutants of *Mycobacterium tuberculosis*. *Antimicrob. Agents*
636 *Chemother.* 59(9):5316-5323.
637 36. Cashmore TJ*, et al.* (2017) Identification of a membrane protein required for lipomannan
638 maturation and lipoarabinomannan synthesis in *Corynebacterineae*. *J. Biol. Chem.*
639 292(12):4976-4986.
640 37. Bashiri G, Rehan AM, Greenwood DR, Dickson JM, & Baker EN (2010) Metabolic engineering
641 of cofactor F420 production in *Mycobacterium smegmatis*. *PLoS ONE* 5(12):e15803.
642 38. Tropea JE, Cherry S, & Waugh DS (2009) Expression and purification of soluble His 6-tagged
643 TEV protease. *High throughput protein expression and purification*, (Springer), pp 297-307.
644 39. Kabsch W (2010) XDS. *Acta Crystallogr. Sect. D.* 66(2):125-132.
645 40. Winn MD*, et al.* (2011) Overview of the CCP4 suite and current developments. *Acta*
646 *Crystallographica Section D: Biological Crystallography* 67(4):235-242.
647 41. Adams PD*, et al.* (2010) PHENIX: a comprehensive Python-based system for macromolecular
648 structure solution. *Acta Crystallogr. Sect. D.* 66(2):213-221.
649 42. Emsley P, Lohkamp B, Scott WG, & Cowtan K (2010) Features and development of Coot. *Acta*
650 *Crystallogr. Sect. D.* 66(4):486-501.

43. Long F*, et al.* (2017) AceDRG: a stereochemical description generator for ligands. *Acta Crystallographica Section D: Structural Biology* 73(2):112-122.
44. Stoessel D*, et al.* (2016) Metabolomics and lipidomics reveal perturbation of sphingolipid metabolism by a novel anti-trypanosomal 3-(oxazolo [4, 5-b] pyridine-2-yl) anilide. *Metabolomics* 12(7):126.

658 Figures

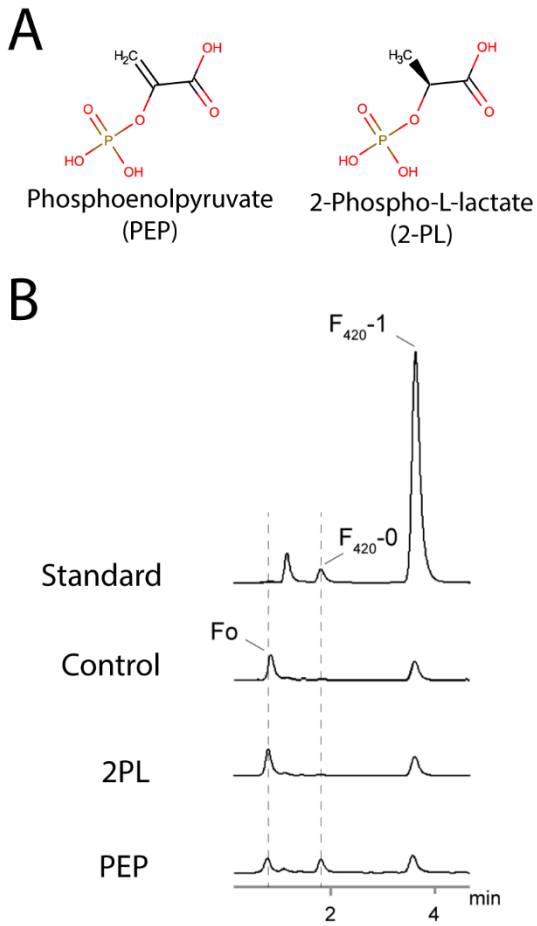

659

660 **Figure 1 PEP but not 2PL stimulates DH-F_{420}-0 synthesis in *M. smegmatis* cell lysates.** (A) 2D
661 structures of PEP and 2PL demonstrating the difference (double bond or single bond) in
662 bonding between carbon 2 and 3. (B) Fluorescence emission detection chromatogram from
663 HPLC of *M. smegmatis* lysates spiked with either 2PL, PEP or an unspiked control. Synthesis of
664 a species with characteristic F_{420} fluorescence (Ex: 420 nm, Em:480 nm) corresponding to F_{420}-
665 0 from the purified standard was only detected in the PEP-spiked lysate. The appearance of
666 this F_{420}-0-like species coincided with a decrease in the presence of Fo, suggesting that PEP is
667 the precursor for F_{420} synthesis in *M. smegmatis* in cells. F_{420}-1 in the standard corresponds to
668 F_{420} with a single glutamate moiety.

669

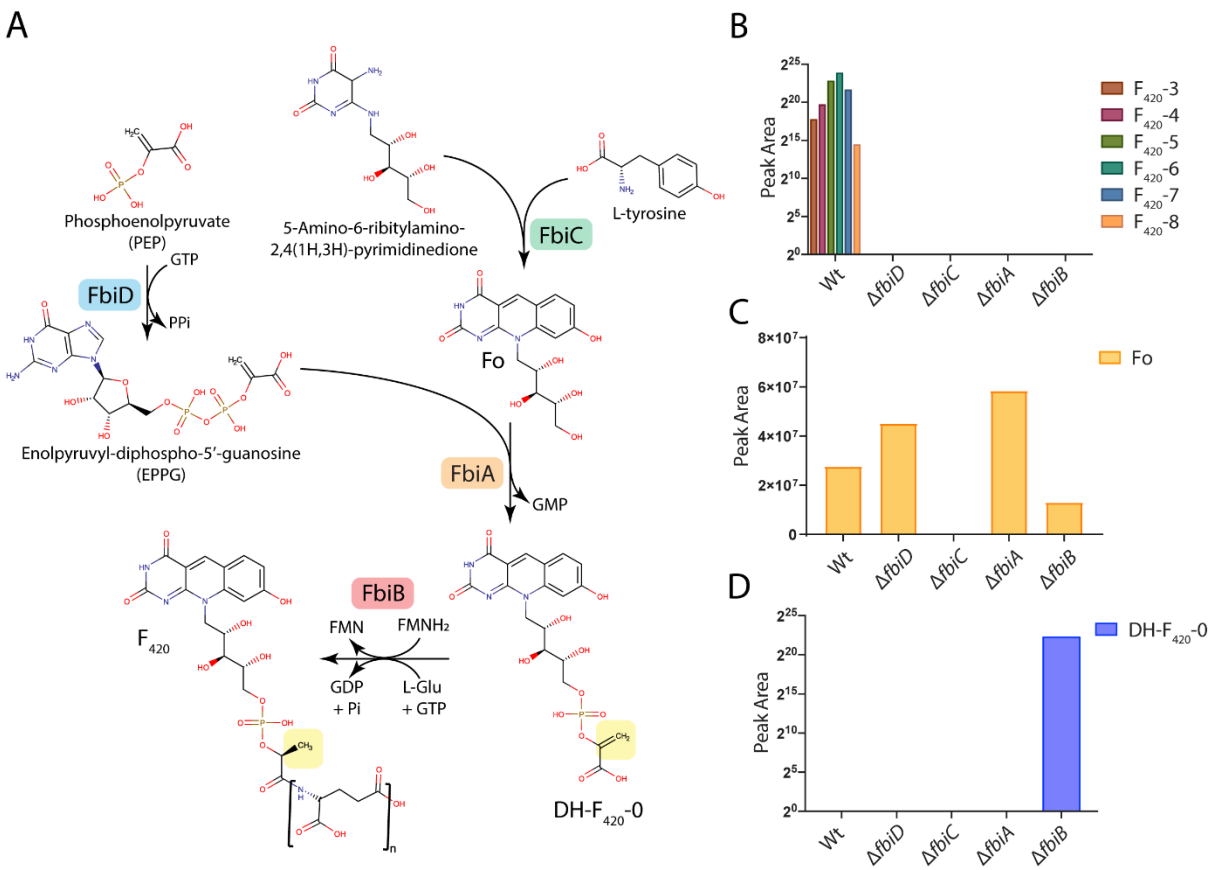

Figure 2 Mutagenic dissection of the F_{420} biosynthesis pathway in *M. smegmatis* reveals DH-F_{420}-0 is the biosynthetic intermediate in mycobacteria. (A) A schematic of the F_{420} biosynthesis pathway in *M. smegmatis* with PEP, rather than 2PL, utilised by FbiD to create the reaction intermediate EPPG. The enzymes responsible for catalytic steps are shown, along with the 2D-structures of proposed pathway intermediates and mature F_{420}. The yellow box highlights the reduction of DH-F_{420}-0, proposed to be mediated by the C-terminal domain of FbiB using $FMNH_2$. LC-MS detection of mature F_{420} species (B), Fo (C) and DH-F_{420}-0 (D) in *M. smegmatis* cell lysates of wildtype and F_{420} biosynthesis pathway mutants confirming the proposed function of the F_{420} biosynthetic genes detecting the novel intermediate DH-F_{420}-0 in whole cells. F_{420}-X species in panel B correspond to different lengths of the ploy-glutamate chain where X = n tail length.

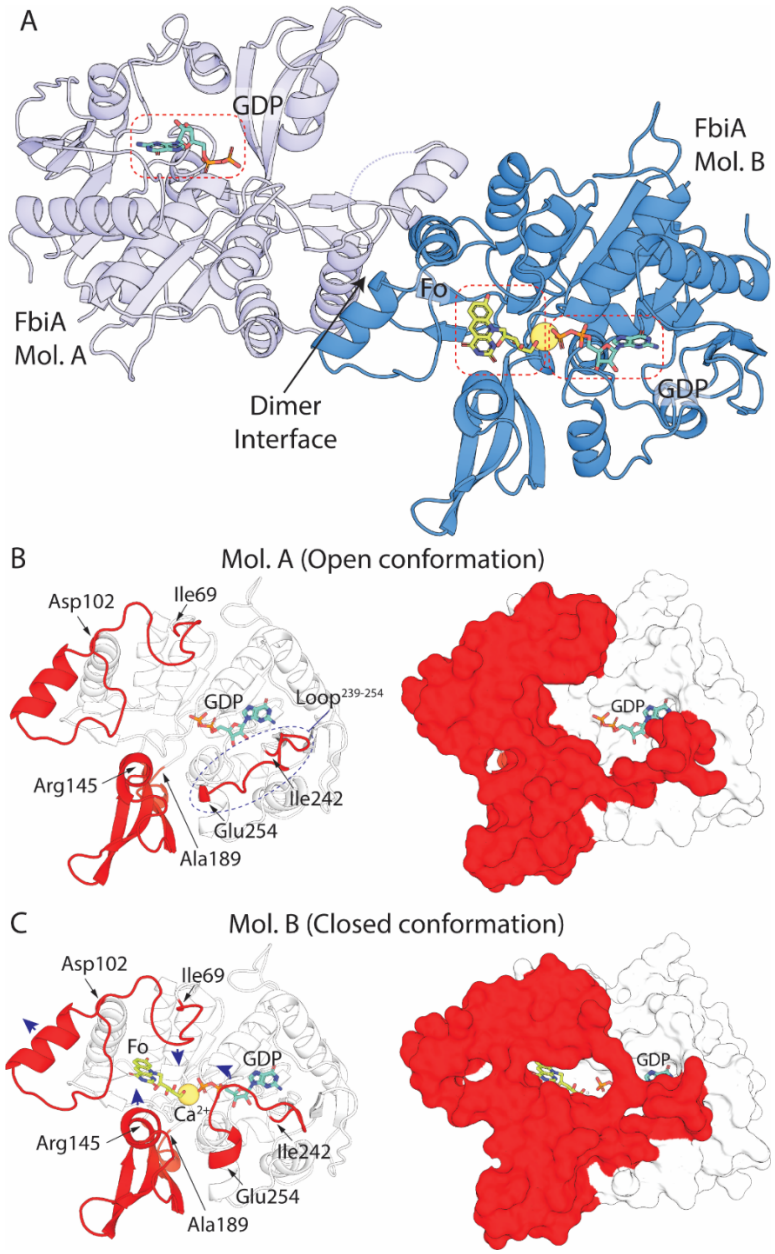

683

684 **Figure 3 The crystal structure of FbiA captures the enzyme in open and closed states.** (A) The
685 crystal structure of FbiA from *M. smegmatis* in complex with Fo and GDP. FbiA is shown as a
686 cartoon representation with Mol. B colored in sky blue and Mol. A colored in light blue. GDP
687 and Fo are shown as a stick representation and Ca^{2+} is shown as a yellow sphere. (B) Mol. A
688 from the FbiA structure exists in an open conformation. Left shows Mol. A as a cartoon with
689 loops and subdomains which differ in conformation in Mol. B highlighted in red. Right shows
690 Mol. A as a surface representation with mobile regions highlighted in red. (C) Mol. B. of FbiA
691 structure exists in a closed 'catalytically ready' state. Left is displayed as panel B, with the
692 direction of movement of loops compared to Mol. A shown with blue arrows. Right shows
693 Mol. B as in panel B, demonstrating how the mobile regions enclose the FbiA active site.

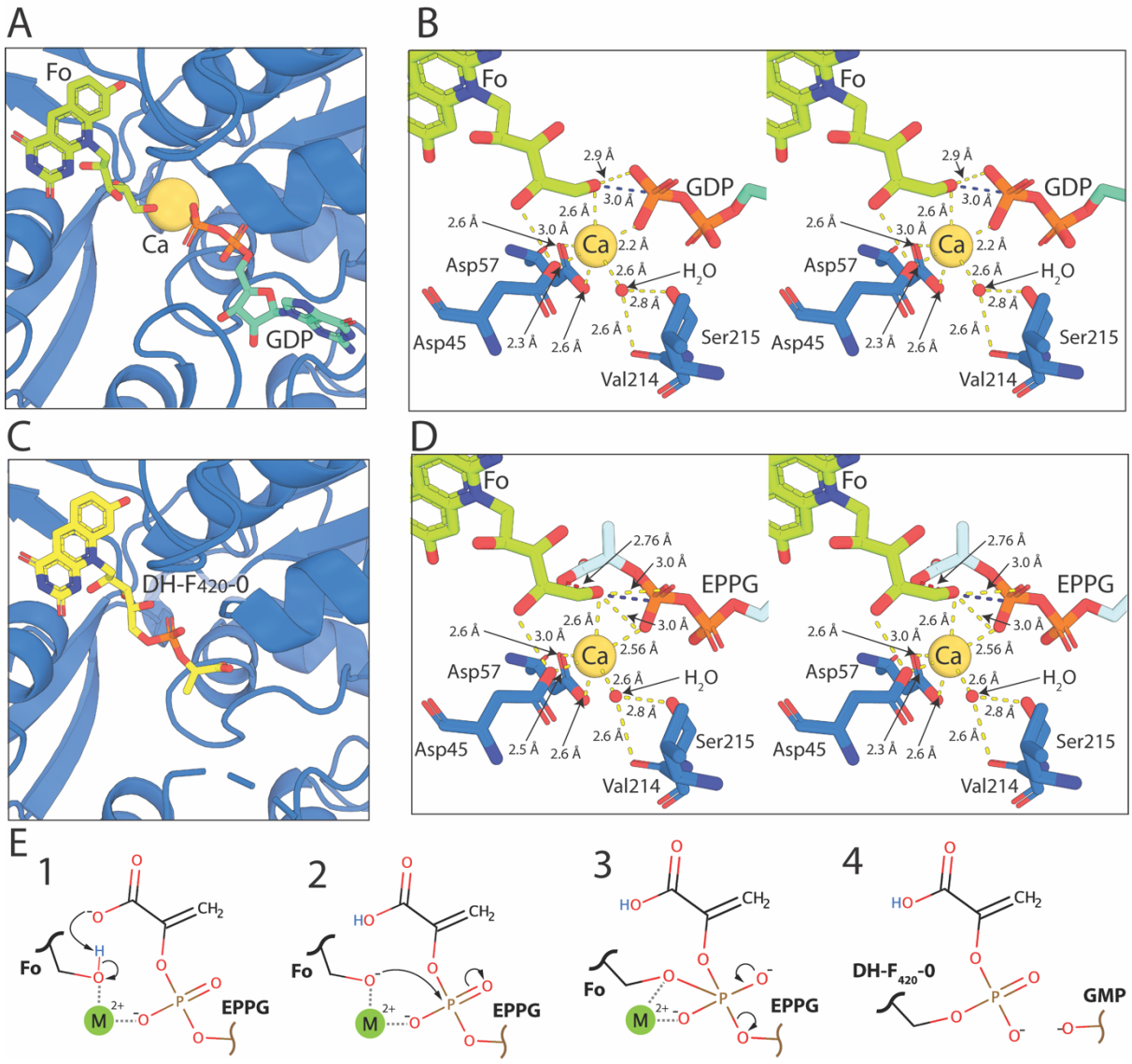

Figure 4 Resolution of the structure of FbiA in the presence of Fo, GDP and DH-F_{420}-0 provides insight into its catalytic mechanism. (A) Fo and GDP in complex with Mol. B of FbiA in coordination with the catalytic Ca^{2+} ion. FbiA is shown as a sky-blue cartoon, Fo and GDP as sticks and Ca^{2+} as a sphere. (B) A stereoview of the catalytic center of the FbiA active site in complex with Fo and GDP, showing FbiA sidechains involved in coordinating the catalytic metal ion and a coordinating H_2O molecule. Bond distances <3.2 Å are shown as yellow dashed lines, the distance between the terminal OH of Fo and P of the β-phosphate of GDP is highlighted in blue. (C) DH-F_{420}-0 in complex with FbiA, shown as in panel A. (D) A stereoview of the FbiA catalytic centre with the reaction substrate EPPG model in place of GDP displayed in panel C, with the close proximity between the carboxylic acid group of EPPG and the terminal OH of Fo highlighted with a red dashed line. (E) A schematic showing the proposed catalytic mechanism for the formation of DH-F_{420}-0 by FbiA.